



## Surface wettability control by nanocoating: The effects on pool boiling heat transfer and nucleation mechanism

Hai Trieu Phan<sup>a,b,\*</sup>, Nadia Caney<sup>a</sup>, Philippe Marty<sup>a</sup>, Stéphane Colasson<sup>b</sup>, Jérôme Gavillet<sup>c</sup>

<sup>a</sup> LEGI, BP 53, 38041 Grenoble Cedex 9, France

<sup>b</sup> LITEN/GRETh, CEA Grenoble, 17 rue des martyrs, 38054 Grenoble Cedex 9, France

<sup>c</sup> LITEN/LTS, CEA Grenoble, 17 rue des martyrs, 38054 Grenoble Cedex 9, France

### ARTICLE INFO

#### Article history:

Received 17 October 2008

Received in revised form 16 June 2009

Accepted 25 June 2009

Available online 5 August 2009

#### Keywords:

Surface wettability

Contact angle

Heat transfer

Nanocoating

Pool boiling

### ABSTRACT

Experiments were performed to highlight the influence of surface wettability on nucleate boiling heat transfer. Nanocoating techniques were used to vary the water contact angle from 20° to 110° by modifying nanoscale surface topography and chemistry. The bubble growth was recorded by a high speed video camera to enable a better understanding of the surface wettability effects on nucleation mechanism. For hydrophilic (wetted) surfaces, it was found that a greater surface wettability increases the vapour bubble departure radius and reduces the bubble emission frequency. Moreover, lower superheat is required for the initial growth of bubbles on hydrophobic (unwetted) surfaces. However, the bubble in contact with the hydrophobic surface cannot detach from the wall and have a curvature radius increasing with time. At higher heat flux, the bubble spreads over the surface and coalesces with bubbles formed at other sites, causing a large area of the surface to become vapour blanketed. The best heat transfer coefficient is obtained with the surface which had a water contact angle close to either 0° or 90°. A new approach of nucleation mechanism is established to clarify the nexus between the surface wettability and the nucleate boiling heat transfer.

© 2009 Elsevier Ltd. All rights reserved.

### 1. Introduction

Nucleate boiling is an effective heat transfer mode which has an important place in engineering disciplines. For several decades, it has been a subject of intensive research. Several models have been developed to predict the bubble initiation, growth and departure. An excellent review of nucleation theory was given by Carey [1]. Although the influence of the surface wettability on the bubble growth and on the heat transfer has early been discussed, it still remains unclear and requires further investigations. Up to now, little experimental data is available about this subject because of the difficulty of varying the contact angle while keeping all other parameters constant. One traditional method to modify the liquid contact angle is the use of surfactant solutions as Wen and Wang [2]. The authors found that the addition of surfactant could enhance the water boiling heat transfer by the change of surface wettability, which had been neglected for a long time and could be an important parameter influencing boiling heat transfer. The disadvantage of this method is to vary both the surface wettability and the surface tension. Hence, the enhancement of the boiling heat transfer

might be due to the significant decrease of the surface tension rather than the increase of the surface wettability. Oxidizing copper is another method widely applied. The surface wettability is modified by controlling the degree of oxidation of the surface. Using this method, Liaw and Dhir [3] found that for a given heat flux, the wall void fraction increases as the surface wettability decreases, whereas the maximum heat flux decreases with an increase in contact angle. However, oxidizing copper may change the surface topography at microscale which is the characteristic scale of nucleation sites. Another method employed by Takata et al. [4] is TiO<sub>2</sub> photocatalysis. The authors observed a significant decrease of water contact angle when the surface coated with TiO<sub>2</sub> is irradiated by UV light. Due to this property of TiO<sub>2</sub>, they made superhydrophilic surfaces of which the heat transfer characteristic in nucleate boiling is better than that of an uncoated one. Though, the study of Takata et al. [4] is limited in contact angle range and stability: the contact angle varied from 0° to 20° and was unstable during experiment.

Furthermore, most experiments on boiling heat transfer dealt with wetted surfaces. Few studies investigated nucleate boiling mechanism on nonwetting material as summarised in the chapter 11 of Webb and Kim [5]. Griffith and Wallis [6] performed experiments on single conical cavities 0.08 mm in diameter, formed by pressing a needle into the boiling surface. They found that unwetted

\* Corresponding author. Address: LEGI, BP 53, 38041 Grenoble Cedex 9, France. Tel.: +33 4 38 78 01 82; fax: +33 4 38 78 55 68.

E-mail address: [hai-trieu.phan@cea.fr](mailto:hai-trieu.phan@cea.fr) (H.T. Phan).

## Nomenclature

$C_d$	drag coefficient
$D$	diameter, m
$h$	heat transfer coefficient, W/m <sup>2</sup> K
$H$	specific enthalpy, J/kg
$\Delta h$	uncertainty in $h$ , W/m <sup>2</sup> K
$I$	current, A
$f(\theta)$	energy factor
$\Delta E_f$	formation energy, J
$F_d$	drag force, N
$F_I$	inertial force, N
$F_g$	gravity force, N
$F_\sigma$	surface tension force, N
$M$	molecular weight, kg/kmol
$p$	pressure, Pa
$p^*$	reduce pressure
$q$	heat flux density, W/m <sup>2</sup>
$\Delta q$	uncertainty in $q$ , W/m <sup>2</sup>
$R_p$	roughness (DIN 4762/1), $\mu\text{m}$
$R^*$	critical cavity radius, m
$S$	external surface area, m <sup>2</sup>
$T$	temperature, K
$\Delta T$	uncertainty in $T$ , K
$U_T$	bubble growth velocity, m/s
$V$	voltage, V

### Greek symbols

$\delta$	thickness, m
$\dot{\delta}$	growth rate, m/s
$\varphi$	nanoparticle volumetric fraction
$\theta$	contact angle at 25 °C, degree or rad
$\theta^*$	contact angle at $T_s$ , degree or rad

$\mu$	dynamic viscosity, Pa s
$\rho$	density, kg/m <sup>3</sup>
$\sigma$	liquid–vapour surface tension, N/m
$\tau_{gt}$	growth time, s
$\tau_{wt}$	waiting time, s

### Subscripts

0	initial
$a$	advancing
$b$	bubble
$B$	base
$cr$	critical
$dp$	departure
$e$	equilibrium
$f$	liquid phase
$fg$	liquid-to-vapour transition
$g$	gas phase
$l$	liquid
$lv$	liquid–vapour
$m$	microlayer
$r$	receding
$s$	saturation
$sl$	solid–liquid
$sv$	solid–vapour
$w$	wall

### Dimensionless numbers

$Bo$	Bond number $\left(\frac{F_g}{F_\sigma}\right)$
$Re$	Reynolds number $\left(\frac{D_b U_T \rho_l}{\mu_l}\right)$

(paraffin-coated) cavities are more stable in term of heat transfer than wetted (clean) ones. Gaertner [7] carried out further work with artificial nucleation sites, covering the inside surface of the cavities with a nonwetting material. The coated cavity surface boiled at a lower superheat and remained active for a much longer time. However, the heat transfer coefficient was considerably reduced if the coating was deposited on the entire surface because of the bubble coalescence that caused the entire surface to become vapour blanketed. Hummel [8] boiled water on a stainless steel surface which had been sprayed with Teflon, producing 30–60 spots/cm<sup>2</sup> with a spot diameter of 0.25 mm or less. The author observed a significant heat transfer enhancement. Gaertner [7] and Hummel [8] argue against the merits of a continuous surface coating because of the tendency of the surface to become vapour blanketed. Nevertheless, Vachon et al. [9] did not observe vapour blanketing when boiling water on stainless steel covered by an 8  $\mu\text{m}$  thick layer of Teflon.

Today, the progress in nanocoating allows modifying the surface wettability without a large change in the surface topography at microscale. Particles of very small size (less than 100 nm) called “nanoparticles” can be deposited on the heated surface. By changing the particles material, it is possible to vary the water contact angle between 0° and 180°. The techniques used in our laboratory are, respectively, “Metal–Organic Chemical Vapour Deposition” (MOCVD), “Plasma Enhanced Chemical Vapour Deposition” (PECVD) and “Nanofluids Nucleate Boiling Deposition” (NNBD). While MOCVD and PECVD are well known techniques, NNBD is relatively new and still requires much investigation in order to become industrially worthy. In fact, nanofluid research over the past 5 years reported a build-up of a thin layer of nanoparticles on the heated surface during nucleate boiling [10–16]. Our recent

work confirms this finding and proves that the nanoparticle layer thickness can be controlled by using the estimation of Kim et al. [12]. Therefore, we denote this technique as “Nanofluids Nucleate Boiling Deposition”. For future works, NNBD is expected to be improved in terms of deposition strength and homogeneity.

In summary, researchers have early recognised surface wettability as a major factor in boiling heat transfer, but they were not able to conduct accurate experiments for lack of technology. Using MOCVD, PECVD and NNBD techniques, we provide for the first time a complete set of experimental data to explore the effects of surface wettability change on the nucleation mechanisms and thereby on the heat transfer coefficient (HTC). Moreover, a new approach to bubble growth during nucleate boiling is established as an insight to understand the experimental results. Preparation and characterisation of the test surfaces are reviewed in Section 2. The experimental apparatus and procedure are described in Section 3. Nucleation pictures and HTC data are presented in the same Section and discussed in the light of the nucleation theories in Section 4. Conclusions are provided in Section 5.

## 2. Coating process and contact angle

The initial surface is made of stainless steel (grade 301) ribbon and has a water contact angle of about 85°. It was cut to make seven sample surfaces 100 mm long, 5 mm wide and 20  $\mu\text{m}$  thick. One of them, called “S-ref”, is used as reference of the uncoated surface. The others were structured either by MOCVD, PECVD or NNBD to get different water contact angle from 22° to 112° (cf. Fig. 1). Prior to coating, these samples were cleaned (acetone washing in ultrasonic bath for 15 min) and dried (compressed air).

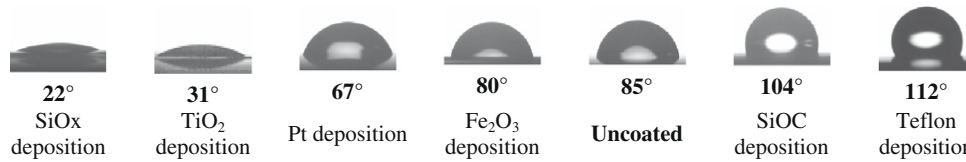


Fig. 1. Static contact angles of 2- $\mu$ l sessile water droplets on stainless steel surfaces with and without nanoparticle deposition.

### 2.1. MOCVD process

Platinum and iron oxide Fe<sub>2</sub>O<sub>3</sub>-based nanocoating materials were prepared by a nonconventional Chemical Vapour Deposition (CVD) process, i.e. Direct Liquid Injection Metal-Organic Chemical Vapour Deposition technique (DLI-MOCVD). The schematic representation of the reactor is shown in Fig. 2 (more details are given in [17,18]). This reactor is a hot-wall reactor fitted with a liquid injection system that allows the generation of a stable gas phase from unstable organometallic compounds with an accurate control of the content of these precursors. Depositions were carried out under low pressure (800 Pa) in the presence of stainless steel sample surface. The surfaces coated by platinum and iron oxide deposition are called “S-Pt” and “S-Fe<sub>2</sub>O<sub>3</sub>”, respectively.

### 2.2. PECVD process

Processes developed at the CEA for hydrophilic and hydrophobic applications are based on the Plasma Enhanced Chemical Vapour Deposition (PECVD) technique. Plasmas are produced inside a cylindrical stainless steel vacuum chamber (diameter 30 cm) with a parallel plate configuration. Substrates to be coated are positioned on the lower grounded electrode. The precursor vapour is uniformly distributed in the reactor by the upper showerhead electrode (with pinholes of 1 mm diameter). The upper electrode is externally connected, through a semi-automated matching network (Dressler VM1000A), to a 13.56 MHz radio-frequency (RF) power supplier (Advanced Energy Cesar<sup>®</sup> RF power supply) which provides a RF voltage with respect to the grounded chamber. Before operating the discharge the device is evacuated to

$5 \times 10^{-3}$  mbar by means of a rotary pump (Alcatel ADS 501). During plasma deposition, the chamber is maintained under void condition by means of the rotary pump.

#### 2.2.1. Hydrophilic coatings

Hexamethyldisiloxane (HMDSO) is a monomer that cannot be polymerised following the conventional polymerisation methods in liquid phase because it does not have cyclic or double bonds in its structure. However, HMDSO can be polymerised during plasma treatments, by rearranging the radicals produced by its dissociation induced by electron impact. Soft coatings of SiO<sub>x</sub>C<sub>y</sub>H<sub>z</sub> with high content of methylene and methyl groups are obtained by using pure HMDSO in plasma process yields. Adding some oxidizing mixture to the plasma chemistry tends to turn these latter groups into hydroxyl groups which are known to be polarised and thus hydrophilic.

#### 2.2.2. Hydrophobic coatings

Unlike HMDSO, octaméthylcyclotétrasiloxane (OMCTS) and octafluorocyclobutane (C<sub>4</sub>F<sub>8</sub>) monomers do have cyclic bonds which enable polymerisation and are also compatible with plasma activation. One advantage of using such precursors is their relatively high content of methyl and fluoromethyl groups and low density which make these materials highly hydrophobic. In the present case, plasma deposition is carried out in a reducing mixture with low plasma activation to preserve methyl and fluoromethyl groups.

The surfaces coated by deposition of SiO<sub>x</sub>, SiOC and Teflon are, respectively, called “S-SiO<sub>x</sub>”, “S-SiOC” and “S-Teflon”.

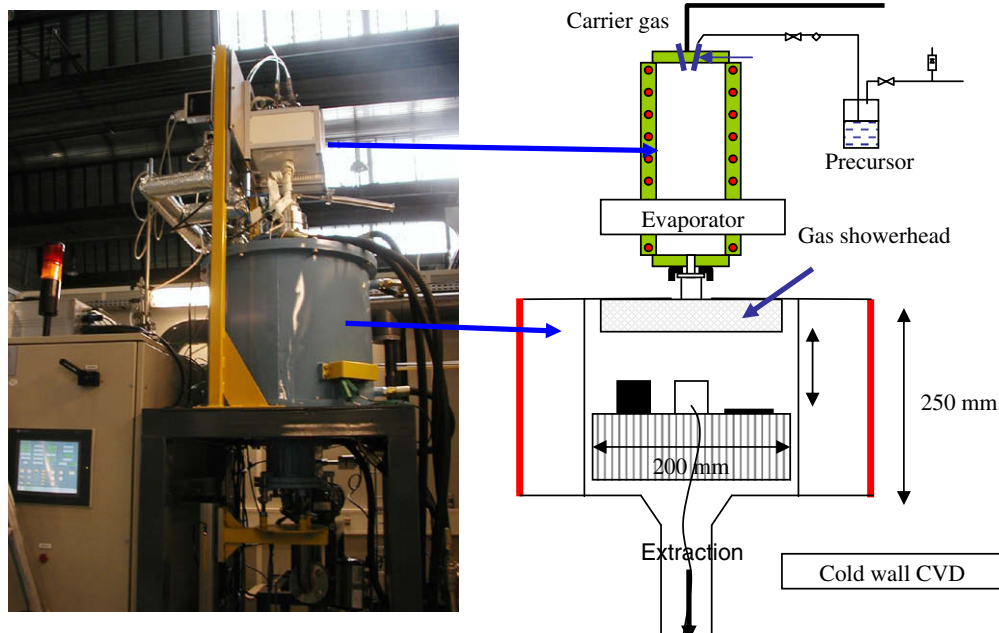


Fig. 2. MOCVD apparatus available at CEA Grenoble and its schematic representation.

### 2.3. NNBD process

The operating principle of NNBD technique is to boil nanofluids by direct heating of the sample surface. Due to liquid microlayer evaporation underneath vapour bubble, nanoparticles deposit on the heated surface. We have selected  $\text{TiO}_2$  nanofluid with nanoparticle size from 10 to 50 nm as a working fluid for this study. The rate of growth of the nanoparticles deposition layer is estimated in [12]:

$$\dot{\delta} = \frac{3}{2} \frac{\delta_m \varphi q}{D_b \rho_g H_{fg}} \quad (1)$$

The surface coated by  $\text{TiO}_2$  nanofluid boiling is called “S- $\text{TiO}_2$ ”. The titanium dioxide nanofluid is made by hydrolysis of titanium alkoxides in absolute ethanol according to the following steps.  $\text{Ti}(\text{OEt})_4$  (Aldrich) is added at room temperature to absolute ethanol under argon. Afterwards, an equimolar quantity of dry triethanolamine (Aldrich) versus titanium alkoxide is added to the latter solution. Then, the yellow solution is stirred at room temperature for 2 h. Finally, an equimolar quantity of deionised water versus titanium alkoxide is added. The solution is again stirred for 2 h at room temperature. A large amount of water is added and the solution is dialysed against deionised water using a regenerated cellulose tubular membrane (Roth, MWCO: 4000–6000) during three days. The titanium dioxide obtained is under rutile phase (XRD). The size of particles measured by dynamic light scattering (Malvern Nanosizer) is in the range of 4–10 nm. However, this size increases with time, after one month the mean diameter is 20–30 nm.

In summary, all tested surfaces except S-ref were coated by one of these three techniques (cf. Table 1). Unlike millimetric and micrometric surface coatings, nanoparticle deposition makes it possible to change significantly the surface wettability without a large change of the surface topography.

### 2.4. Surface characterisation and water contact angle

In order to benchmark surface topography changes induced by nanoparticles deposition, AFM (Atomic Force Microscope)

scanning of the uncoated surface was carried out in a  $10 \mu\text{m} \times 10 \mu\text{m}$  representative area of the sample (cf. Fig. 3). The scan shows surface machining patterns in the shape of parallel micro-grooves with an average period of around  $5 \mu\text{m}$  and an apparent depth equivalent to a mean roughness of 30 nm. It is then expected that nanoparticles deposit with a thickness lower in scale than the uncoated sample roughness will not affect nucleation. Table 1 shows that surface coatings satisfy this condition in the cases of PECVD and MOCVD processes. In addition, qualitative analysis was performed by Field-Emission Gun Scanning Electron Microscopy (FEG-SEM) as shown in Fig. 4. We observe that the surfaces with non-continuous layer of nanoparticles deposition (S- $\text{TiO}_2$ , S-Pt and S- $\text{Fe}_2\text{O}_3$ ) seem to be quite homogenous and their topographies are changed in nanometric scale only. Beyond, as a result of very thin nanoparticle layer deposition, the topographies of the surfaces coated by PECVD technique (S-SiOx, S-SiOC and S-Teflon) remain similar to that of the uncoated surface.

To quantify the wettability of the sample surfaces, the static contact angle  $\theta$  was measured at  $25^\circ\text{C}$  in air by using the sessile drop technique with the following steps. First, a  $2\text{-}\mu\text{l}$  sessile droplet is deposited by a syringe pointed vertically down onto the sample surface. Then, a high resolution camera captures the image, which will be analysed by image analysis software. Hence, the static contact angle is determined. These steps were achieved by using KRÜSS EasyDrop systems. For a sample surface, the static contact angle is the mean value of the static contact angles measured at twenty different points uniformly distributed on the surface (five measurements are made at each point). The uncertainty on such measurements is estimated to be  $\pm 5^\circ$ . Low values of the contact angle correspond to high surface wettability. Fig. 1 presents the contact angle data window and corresponding water droplet images. We notice that the surfaces with SiOC or Teflon deposition are hydrophobic ( $\theta > 90^\circ$ ) and the surface with SiOx deposition has the highest wettability. Hence, the static contact angle can be significantly changed by the addition of nanoparticles of different materials on the initial surface.

**Table 1**  
Tested surfaces characteristics.

Surface name	Deposition particle	Deposition technique	Deposition type
S-SiOx	SiOx	PECVD	Continuous monolayer of 20 nm thickness
S- $\text{TiO}_2$	$\text{TiO}_2$	NNBD	Non-continuous multilayer of 100 nm thickness
S-Pt	Pt	MOCVD	Non-continuous monolayer 20 nm thickness
S- $\text{Fe}_2\text{O}_3$	$\text{Fe}_2\text{O}_3$	MOCVD	Non-continuous monolayer 20 nm thickness
S-ref	–	–	–
S-SiOC	SiOC	PECVD	Continuous layer of 20 nm thickness
S-Teflon	Teflon	PECVD	Continuous layer of 20 nm thickness

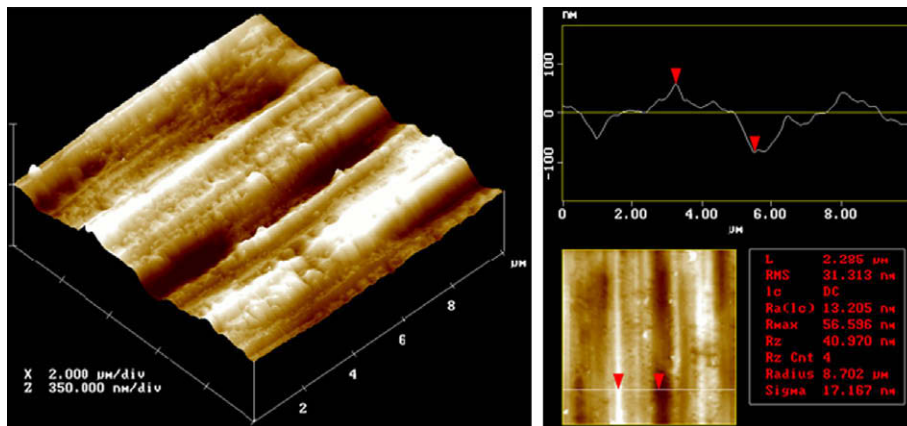


**Fig. 3.** AFM topography of the uncoated surface S-ref. It is composed of successive grooves of  $5 \mu\text{m}$  width and 110 nm depth.

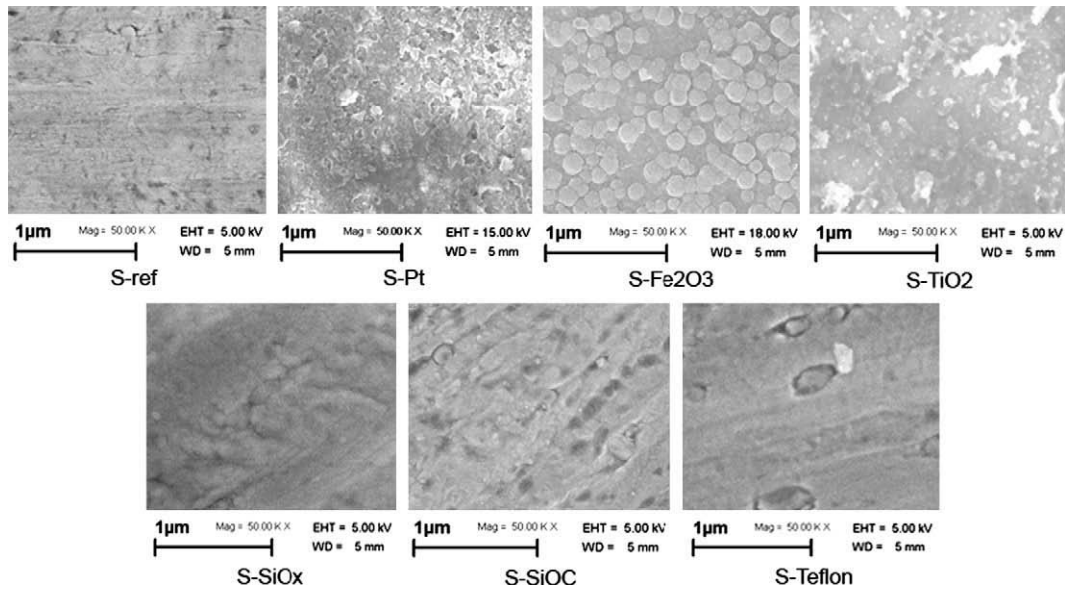


Fig. 4. FEG-SEM images of the tested surfaces (by MOCVD: S-Pt and S-Fe<sub>2</sub>O<sub>3</sub>; by NNBD: S-TiO<sub>2</sub> and by PECVD: S-SiOx, S-SiOC and S-Teflon).

### 3. Pool boiling

#### 3.1. Experimental apparatus

The experimental pool boiling setup is presented in Fig. 5. The layout is designed to study the pool boiling heat transfer in a horizontal position with clean or deposited surfaces. The main components are a test foil heater (1), a boiling vessel (2), a sample holder (3) and a thermostat (4). The test foil heater (1) is made of stainless steel 301 and its faces 100 mm × 5 mm are maintained horizontally by the sample holder (3) fixed inside the boiling vessel (2). A DC power supply (30 V–20 A) is connected to the test foil for Joule heating. The thermostat (4) is provided for initial heating of water and maintenance of the water bulk temperature at 85 °C. Water enters and leaves of the boiling vessel at very low flow rate to avoid disturbing the local pool boiling. Before each measurement, the test foil is heated to a temperature higher than that of the saturate temperature, thereby several gasses trapped inside the test foil surface are removed. During experiment, the boiling process was captured by a high speed camera to promote a better understanding of the surface wettability effects. The recording speed of the camera has been set at 6000 fps.

The test foil surface is either in its original state or coated (cf. Section 2). In both cases, its electrical resistance was previously calibrated. In this study, the test foil was put inside a thermostat of which the temperature was measured by a platinum probe of 0.1 °C accuracy. At steady state, the temperature of the test foil could be determined from the temperature of the thermostat. For temperature between 25 and 90 °C, the test foil electrical resistance was determined by 4-wire measurement method. In this way, the surface temperature  $T_w$  can be deduced from measurements of the electric resistance by using the electrical resistance/temperature curve. Voltage and current are measured by Agilent 3458 A multimeter and a 0.01 Ω shunt. The uncertainty of  $T_w$  is ±1 °C. In addition, a K-type thermocouple of 1.1 °C accuracy is used to measure the fluid bulk temperature.

#### 3.2. Experimental results

##### 3.2.1. Hydrophobic surfaces

Fig. 6 presents some captured images of boiling process on the hydrophobic surfaces (S-SiOC and S-Teflon) of which the static con-

tact angles at 25 °C are, respectively, 104° and 112°. Compared to standard surfaces which are usually wetted, the bubbles appeared on hydrophobic surfaces at very low heat flux and then remained on the surfaces. By increasing the heat flux, the bubble size increased but the bubbles still did not detach from the wall. At higher heat flux, the bubbles spread over the surface, causing bubble coalescence that led to film boiling. No bubble emission was observed on hydrophobic surfaces. This phenomenon could be due to the effect of the surface tension force which will be discussed in detail in Section 4. It could also be due to condensation occurring at the bubble head by highly subcooled liquid. Indeed, condensation reduces the bubble volume and thereby reduces the buoyancy force acting on the bubble to move it upward. However, the bubble volume decrease caused by vapour condensation should be neglected compared to the bubble volume increase caused by evaporation of liquid underneath the bubbles. This is mainly due to the high water liquid to vapour density ratio (at saturate temperature,  $\rho_l/\rho_g \approx 1600$ ).

The surface S-Teflon with higher static contact angle had a greater bubble base radius at the same heat flux. We also observed that film boiling appeared at lower heat flux on higher contact angle surfaces: 120 kW/m<sup>2</sup> for S-Teflon versus 200 kW/m<sup>2</sup> for S-SiOC. These observations agree with that of Gaertner [7] and Hummel [8]: a continuous hydrophobic surface tends to become vapour blanketed during nucleate boiling. However, no bubble departure was noticed and the heat transfer was not stable because of the bubbles remaining on the surface. The wall temperature increased during boiling time and after about 15 min, local wall destruction occurred. Thus, it was impossible to measure the heat transfer coefficient in steady state regime.

##### 3.2.2. Hydrophilic surfaces

###### 3.2.2.1. Bubble size.

The bubble departure diameter is determined by analysing the pictures taken from the video recorded by the high speed camera. Kolev [19] showed that the bubble departure diameter significantly depends on the heat flux. Hence, to strictly determine its dependence on the contact angle, the bubble departure diameter was measured at a constant heat flux of 200 kW/m<sup>2</sup> for every hydrophilic surface. Fig. 7 shows that the bubble departure size increases with the increase of the surface wettability. For very wetted surfaces ( $\theta \leq 31^\circ$ ), the bubble grew and spread over the wall. Contrary to Fritz correlation [20] where the bubble diameter is proportional to the static contact angle, our experimental results (cf.

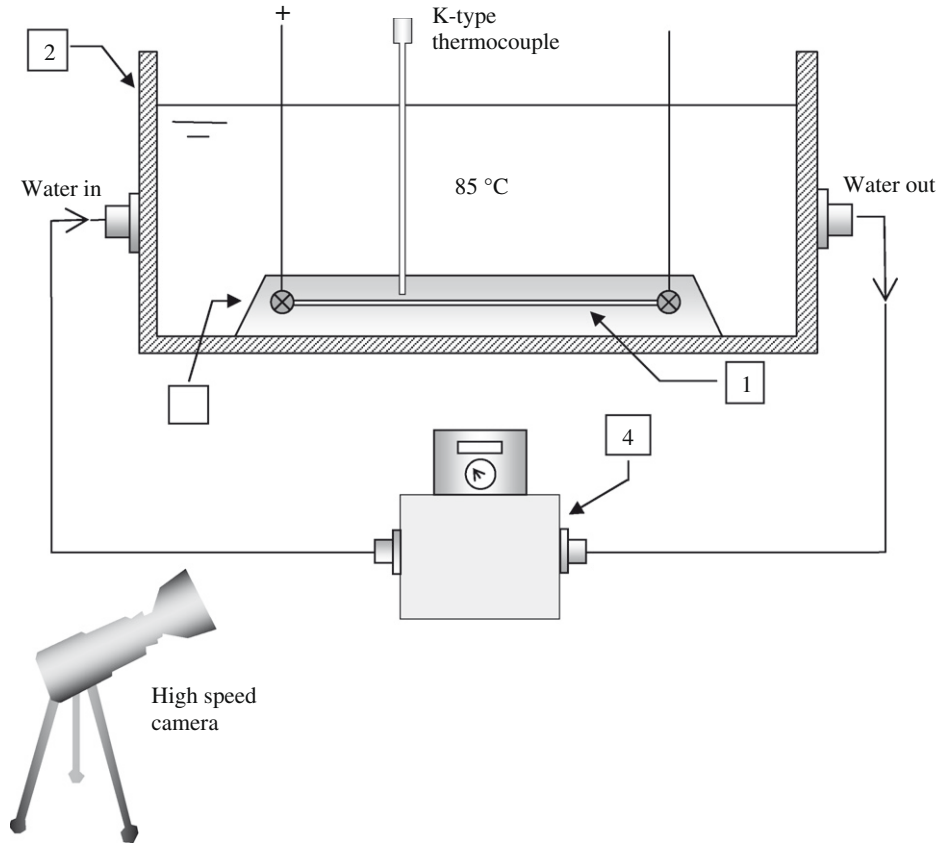


Fig. 5. Schematic view of experimental setup.

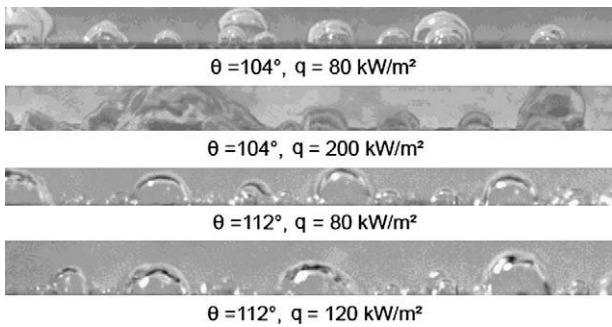


Fig. 6. For hydrophobic surfaces, bubbles are created at lower superheat but cannot detach from the wall. There is no nucleation and film boiling occurs because of bubble coalescence.

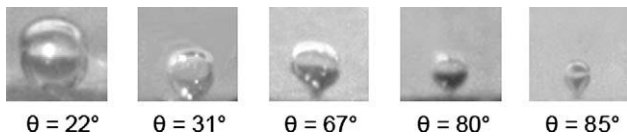


Fig. 7. Bubble departure on hydrophilic surfaces.

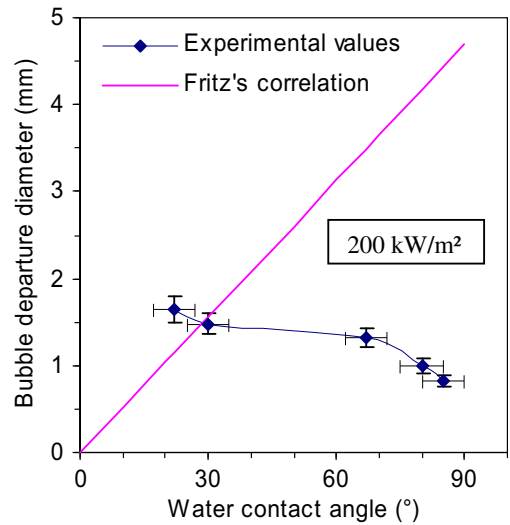


Fig. 8. Bubble departure diameter (measured at 200 kW/m<sup>2</sup>) versus the static contact angle at 25 °C. Fritz's correlation has the opposite tendency compared to the experimental values.

Fig. 8) show that a greater surface wettability yields bigger bubbles detached from the surface. The expression of the Fritz correlation [20] is written as:

$$D_{ap} = 0.020 \times \theta \times \left( \frac{\sigma}{g(\rho_l - \rho_g)} \right)^{1/2} \quad (2)$$

It is important to note that in his paper, Fritz [20] only showed that there is a maximum volume of a vapour bubble, which can be written as a function of contact angle and capillary length, and Eq. (2) does not even appear in this publication. Even though the Fritz correlation [20] is well known and has been used in many studies, it was not validated by a large set of experimental data in boiling conditions where only the surface wettability changed. Fritz [20] confirmed his correlation by measurements with air bubbles and not

with vapour bubbles in boiling conditions. Furthermore, in most studies, the main parameters were: superheat, pressure, gravity and fluid characteristics, and the contact angle was seldom reported. A complete review on bubble departure diameter measured in boiling systems was given by Zeng et al. [21]. It was shown that Eq. (2) gives questionable results for well-wetting fluids, large range of operating pressures and in microgravity conditions. Taking into account our recent results, we present in the next section a new correlation aimed at estimating the bubble departure diameter.

**3.2.2.2. Bubble emission frequency.** The bubble emission frequency  $f$  at a nucleation site is defined as:

$$f = \frac{1}{\tau_{gt} + \tau_{wt}} \quad (3)$$

where  $\tau_{gt}$ , called “growth time”, is the duration of the bubble growth and  $\tau_{wt}$ , called “waiting time”, is the duration between the departure of the former bubble and the appearance of the current bubble. They are determined from the nucleation videos captured at 6000 frames per second.

Fig. 9 shows that the waiting time is much greater than the growth time. This might be due to high liquid subcooling as the bulk temperature is 15 °C below the saturated temperature [22]. Also, the waiting time reduces more rapidly with the increase of the heat flux compared to the growth time. Indeed, the change of the heat flux from 220 to 300 kW/m<sup>2</sup> results in 70% mean decrease of the waiting time but only 23% mean decrease of the growth time. Moreover, the waiting time and the growth time both increase with the rise of the surface wettability. When the static contact angle is below 30°, this effect becomes especially significant. As a result, the bubble emission frequency deteriorates for a greater surface wettability (cf. Fig. 10).

Many studies [23–26] show the higher the bubble emission frequency, the lower the bubble departure diameter. This is in agreement with the trend shown in Figs. 8 and 10.

**3.2.2.3. Heat transfer coefficient (HTC).** The local boiling heat transfer coefficient is defined as:

$$h = \frac{q}{T_w - T_s} \quad (4)$$

where  $q$  is the heat flux calculated from  $q = \frac{V}{S}$  and  $T_s$  is the water saturation temperature at atmospheric pressure, which is measured

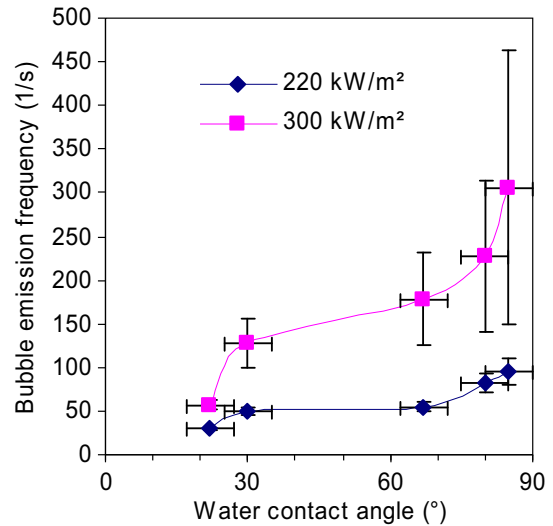


Fig. 10. Bubble emission frequency.

by a mercury barometer. From the uncertainties in test foil length, test foil width, voltage, current and pressure, the uncertainties in the derived parameters ( $q$ ,  $T_s$ ,  $T_w$  and  $h$ ) are estimated using the law of propagation of maximum uncertainty (cf. Table 2). For example, the relative uncertainty in the heat transfer coefficient is calculated as:

$$\frac{\Delta h}{h} = \frac{\Delta q}{q} + \frac{\Delta T_w + \Delta T_s}{T_w - T_s} \quad (5)$$

$$\frac{\Delta h}{h} = \frac{\Delta V}{V} + \frac{\Delta I}{I} + \frac{\Delta S}{S} + \frac{\Delta T_w + \Delta T_s}{T_w - T_s} \quad (6)$$

Voltage and current are accurately measured. Indeed, the maximum uncertainties in the voltage and the current are 0.011% and 0.015%, respectively. The saturate temperature is determined from measurement of atmospheric pressure. Its maximum uncertainty is about 0.2 °C. The wall temperature is determined from electrical resistance/temperature calibration. The uncertainty in the wall temperature is calculated to be less than 1 °C. Uncertainty in the heat transfer coefficient is mainly attributed to uncertainties in wall temperature and surface area.

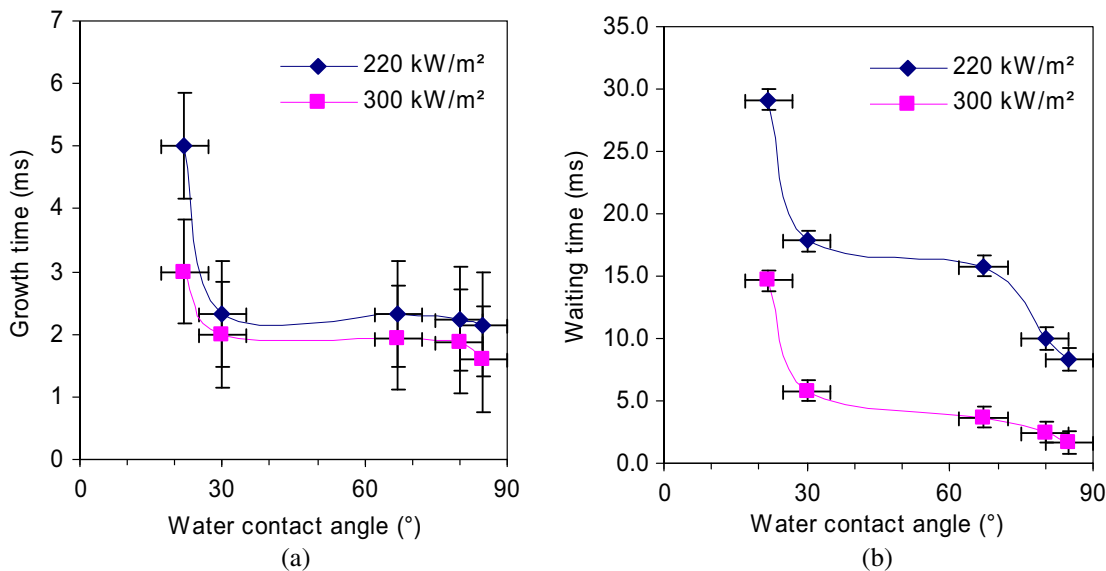


Fig. 9. Evolution of growth time (a) and waiting time (b) as a function of contact angle.

**Table 2**  
Operation conditions and uncertainties.

Parameter	Operational range	Uncertainty
$S$ (cm <sup>2</sup> )	10	3%
$V$ (V)	5–20	0.008–0.011%
$I$ (A)	5–20	0.010–0.015%
$P$ (bar)	1	±0.01
$T_s$ (°C)	100	±0.2
$T_w$ (°C)	100–150	±1
$q$ (kW/m <sup>2</sup> )	50–400	3%
$h$ (W/m <sup>2</sup> K)	3000–16,000	10–20%

Fig. 11 depicts the comparison of experimental values and predictions given by Cooper [27] correlation for the test foil without nanoparticles deposition. The Cooper equation developed for

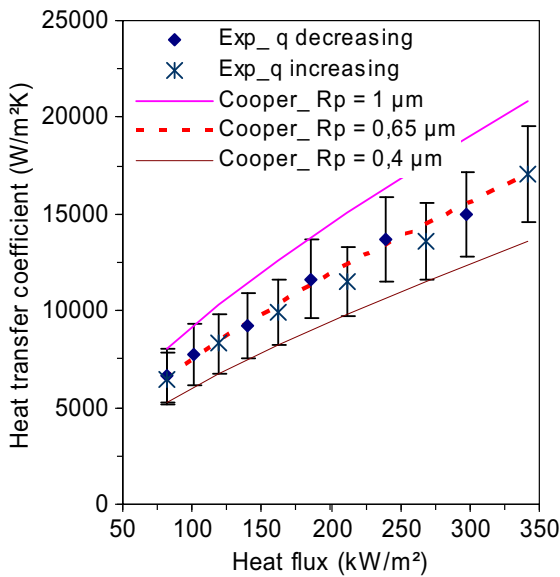
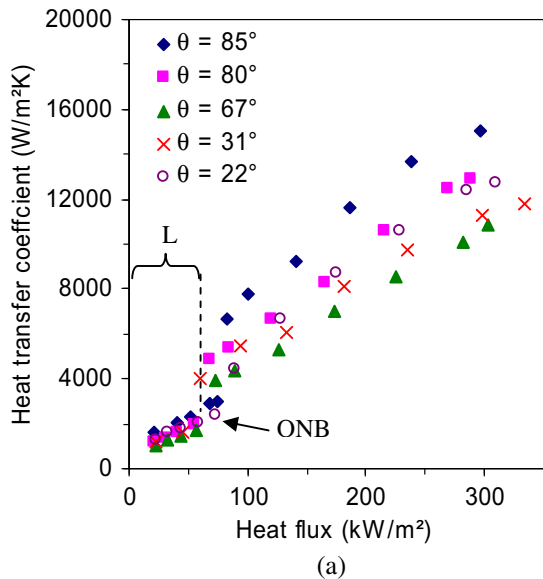


Fig. 11. Heat transfer coefficient of an untreated stainless steel surface.



nucleate pool boiling, accounts for heat flux, surface roughness and reduced pressure effects as follows:

$$h = 55p^{*0.12-0.2\log_{10}R_p} (-\log_{10}p^*)^{-0.55} q^{0.67} M^{-0.5} \quad (7)$$

where  $p^* = p/p_{cr}$  is the reduced pressure,  $R_p$  is the roughness as defined in German standard DIN 4762/1,  $q$  the heat flux density and  $M$  the molecular weight of the fluid. The roughness is chosen to be 0.4, 0.65, and 1  $\mu\text{m}$ , respectively, to fit the experimental values. The changing tendencies of the measured and correlated heat transfer coefficients as a function of the heat flux show a very good coherence, therefore guarantying the reliability of our measurements. Nevertheless, the Cooper correlation should not be used to predict the surface roughness while accounting  $R_p$  as the representative of the number of nucleation sites (cf. Fig. 5). Indeed, Cooper considered that a greater value of  $R_p$  promotes a larger number of nucleation sites on the surface but this assumption has not been proved.

Fig. 12a compares the heat transfer performance of subcooled pool boiling on the hydrophilic surfaces. The tendency of the presented curves is relatively good and shows a significant change of the HTC by the surface wettability change. Fig. 12b highlights this observation and shows that the best HTC is obtained with the surface that has a static contact angle close to either 0° or 90°. Indeed, fitted curves were plotted for experimental data at heat flux from 90 to 290 kW/m<sup>2</sup>. Their extensions at 0° reach relatively well the experimental data of Takata et al. [4] (except at 90 kW/m<sup>2</sup>). Therefore, our results seem to confirm the finding of Takata et al. [4]: the superhydrophilic surface exhibits excellent heat transfer characteristics in nucleate boiling.

**4. Data interpretation**

*4.1. Dynamic contact angle approach for nucleation*

The videos recorded by the high speed camera showed a progressive change of the contact angle during the bubble growth (cf. Fig. 13). As the test surfaces have small deep cavities (cf. Fig. 3), we assume that water wets the working surface completely during experiment (Wenzel [28] model). Hence, a new mechanism of bubble formation during nucleate boiling has been developed and is now presented as follows (cf. Fig. 14):

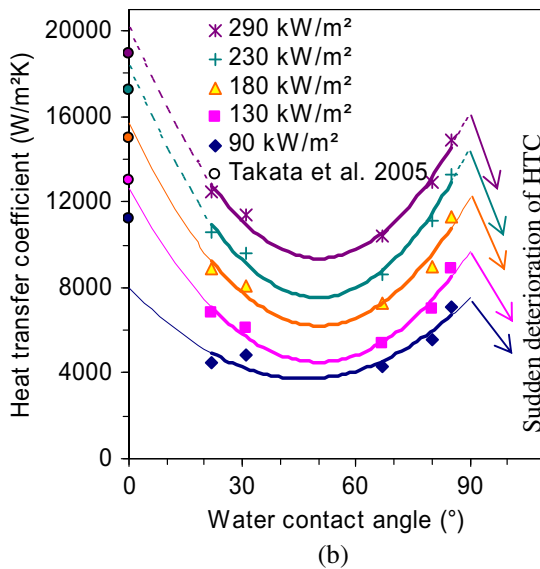


Fig. 12. Effects of the surface wettability on the heat transfer coefficient (L, liquid phase and ONB, onset of nucleate boiling).

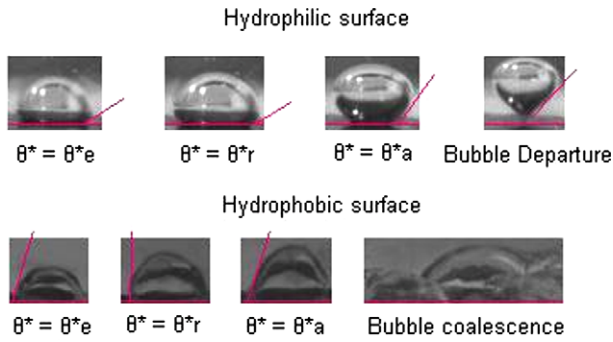


Fig. 13. Contact angle change during growth time ( $\theta_r^* \leq \theta_e^* \leq \theta_a^*$ ).

4.1.1. Hydrophilic surface

- Step 1: A convex vapour shape appears at the cavity base. The contact angle is the equilibrium angle at saturated temperature  $\theta_e^*$ .
- Step 2: The liquid continues evaporating to form a bubble at the cavity mouth. The contact angle is still equal to  $\theta_e^*$ .
- Step 3: The liquid microlayer underneath the bubble evaporates, expanding the triple contact line (TCL) and the bubble diameter. Thus, the liquid recedes from the cavity and the contact angle decreases to the receding angle at saturated temperature  $\theta_r^*$ .
- Step 4: The gravity force stretches the bubble vertically when the liquid moves towards the cavity. The TCL reduces and the contact angle increases to the advancing angle at saturated temperature  $\theta_a^*$ .
- Step 5: The bubble detaches from the wall.

4.1.2. Hydrophobic surface

- Step 1: A concave vapour shape is formed at the cavity base. Its contact angle is equal to the equilibrium angle  $\theta_e^*$ .
- Step 2: The bubble appears at the cavity mouth by the liquid evaporation. The contact angle remains constant but this time the vapour shape becomes convex.
- Step 3: The gravity force increases the bubble height, moving the liquid backward. The contact angle decreases to the receding angle  $\theta_r^*$ . As the latter is greater than  $90^\circ$ . Hence, the bubble cannot detach from the wall.
- Step 4: The liquid moves toward the cavity, increasing the contact angle to the advancing angle  $\theta_a^*$ .
- Step 5: The liquid continues evaporating, expanding the TCL. Hence, the bubble coalesces with bubbles formed at neighbouring sites. Critical heat flux is reached by low vapour conductivity.

4.2. Surface tension force map

Using the dynamic contact angle approach, we may establish the qualitative evolution of the vertical component of the surface tension force with the contact angle to better understand the observed phenomenon (cf. Fig. 15).

The expression of this component which applied vertically to the bubble to maintain it on the wall is expressed as:

$$F_\sigma = \pi D_B \sigma \sin \theta^* \tag{8}$$

where  $D_B$  is the base diameter of the bubble which is equal to that of the TCL.

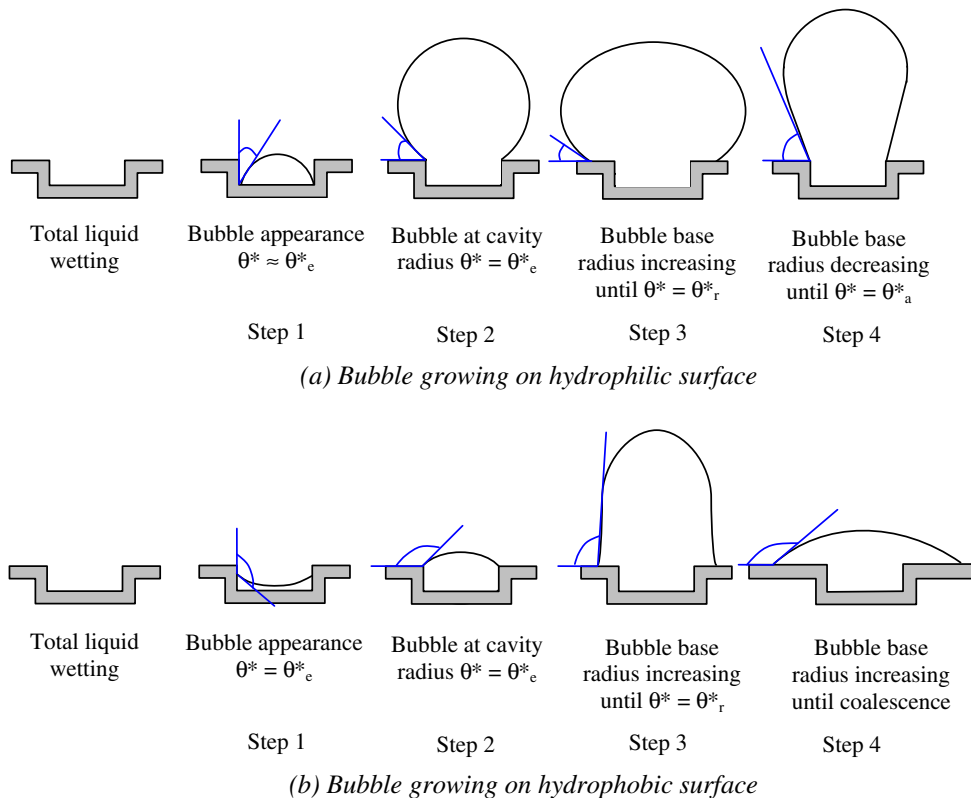


Fig. 14. Dynamic contact angle approach for nucleated boiling.

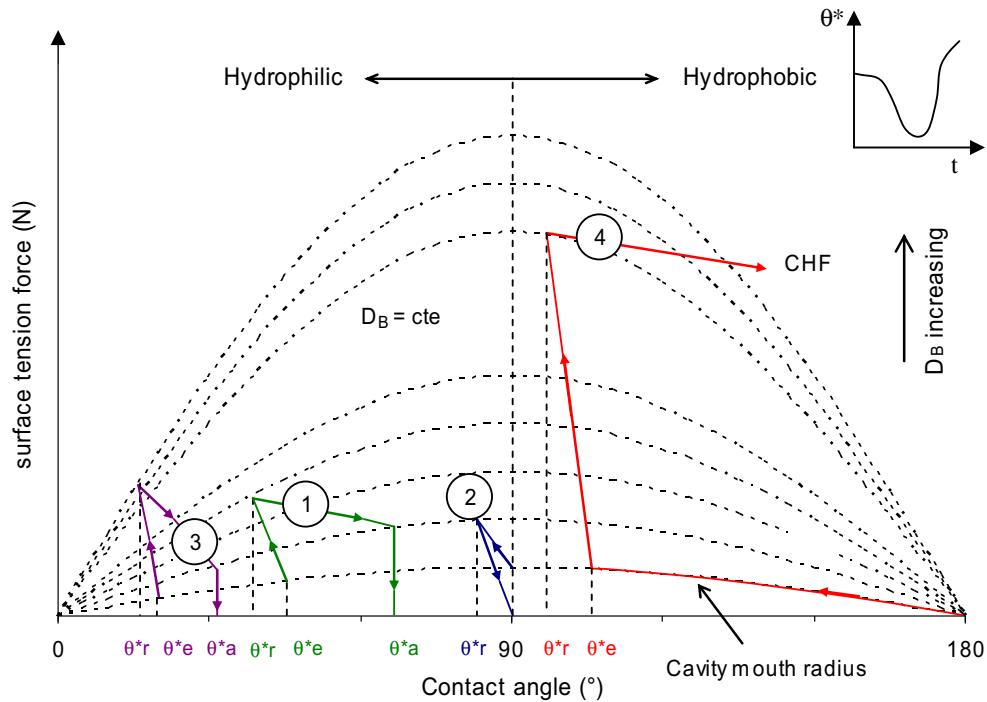


Fig. 15. Dynamic contact angle approach for nucleated boiling.

#### 4.2.1. Hydrophilic surface (curve no. 1–3)

The bubble appears at the cavity mouth and has the cavity mouth diameter as its base diameter. The contact angle is the equilibrium angle  $\theta_e^*$ . Then, the bubble grows when its base diameter increases and the contact angle decreases to the receding angle  $\theta_r^*$ . Therefore, the surface tension force increases to the maximal value. After that, the base diameter reduces and the contact angle increases to the advancing angle  $\theta_a^*$ , decreasing the surface tension force. Finally, the bubble grows vertically: its base diameter reduces to zero while the contact angle remains constant at  $\theta_a^*$ . Thus, the surface tension force is zero and the bubble detaches from the wall. There are two particular cases:

- **Poorly wetted surface** ( $\theta_e^* \approx 90^\circ$ , curve no. 2): After its appearance at the cavity mouth, the bubble grows slightly when the contact angle decreases to the receding angle. Then, its base diameter reduces to zero and it detaches from the wall at the contact angle close to  $90^\circ$ .
- **Highly wetted surface** ( $\theta_e^* \leq 30^\circ$ , curve no. 3): As the contact angle is weak, the bubble diameter is greater for the same surface tension force compared to that of the first case.

#### 4.2.2. Hydrophobic surface (curve no. 4)

Before the appearance of the bubble at the cavity mouth, the vapour shape changes from concave form into convex form: the contact angle reaches  $180^\circ$ . The surface tension force at this angle is zero. As the contact angle decreases to the equilibrium angle  $\theta_e^*$ , the surface tension force intensifies. After that, the bubble diameter increases significantly and the contact angle reduces to the receding angle  $\theta_r^*$  which is greater than  $90^\circ$ . Then, the TCL is expanded by the liquid moving toward the cavity. The bubble cannot detach from the wall as the contact angle increases to  $180^\circ$ . The wall temperature rises violently due to poor conductivity of the vapour. Furthermore, the bubbles coalesce, leading to film boiling. Therefore, critical heat flux is rapidly reached with hydrophobic surface.

#### 4.3. New correlation to estimate the bubble diameter departure

In Sections 4.1 and 4.2, we have showed how a bubble is formed on hydrophilic surface and why it cannot detach from hydrophobic surface. This section aims at highlighting the influences of the wettability on bubble departure diameter and bubble emission frequency. According to the classical nucleation theory [20], the bubble departure diameter of a lower contact angle liquid is smaller because of the lower surface tension force. Fig. 16 illustrates this theory by showing that the modified Bond number, which is the ratio of the surface tension force and the gravity force:  $F_\sigma/F_g$ , increases with the increase of the contact angle. Here, the bubble is assumed to have spherical shape (cf. Fig. 17). Thus, the gravity force is:

$$F_g = g(\rho_l - \rho_g) \frac{\pi D_b^3}{6} f(\theta) \quad (9)$$

where  $f(\theta)$  is the volume ratio of a sphere which has a contact angle  $\theta$  and a full sphere. The surface tension force is calculated by Eq. (8) with:

$$D_B = D_b \sin \theta \quad (10)$$

As shown in Fig. 16, the high ratio of the surface tension force compared to the gravity force is the main reason for the non-detachment of bubble from hydrophobic surfaces. However, for hydrophilic surfaces, the tendency of the bubble departure diameter given by the Bond number analysis does not agree with the experimental results shown in Section 3.2.2. Thereby, the vertical component of the surface tension force should not be considered as the only force which maintains the bubble on the surface. Indeed, the bubble growth by liquid evaporation leads to liquid moving, generating reaction forces (or dynamic forces) exerted by the liquid against the vapour movement: when the bubble volume increases (step 1–3 of Section 4.1), these reaction forces push the bubble toward the wall and inversely when the bubble volume decreases (step 4 of Section 4.1), they pull the bubble in order to detach it from the wall. Drag and inertial forces are examples of liquid reaction forces. They can be simply approximated as:

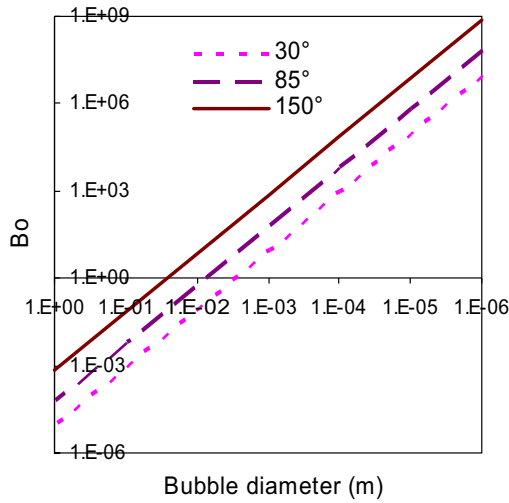


Fig. 16. Bond number decreases with the decrease of the contact angle.

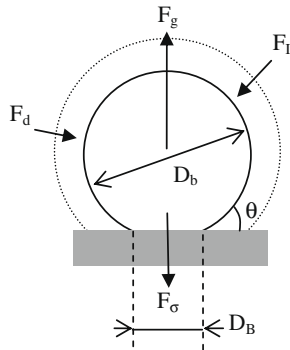


Fig. 17. Forces due to gravity, surface tension, liquid inertia and liquid viscosity.

$$F_d \approx \frac{1}{8} \pi D_b^2 C_d \rho_l U_T^2 \quad (11)$$

$$F_i \propto \rho_l D_b^2 U_T^2 \quad (12)$$

where  $U_T$  is the bubble growth speed and  $C_d$  is correlated by Peebles and Garber equation [29] as:

$$C_d = 18.7 Re^{-0.68} \quad \text{for } Re \geq 2 \quad (13)$$

Indeed,  $U_T$  can be estimated by  $D_{ap}/\tau_{gr}$  and has an approximate value of 1 m/s. Thus, the Reynolds number is close to 3000 with water at 100 °C ( $\mu_l \approx 0.3 \times 10^{-3}$  Pa s) when  $D_b$  is equal to 1 mm. Fig. 18 shows that liquid reaction forces are not negligible and should be taken into account in the force balance. Furthermore, with the enhancement of the surface wetting, experimental data shows that the growth velocity of the bubble augments, increasing the dynamic forces. Therefore, a lower static contact angle leads to a greater bubble departure diameter through its effects on the liquid reaction forces.

In summary, evaporation phenomenon plays an important role in highly subcooled liquid nucleation by generating significant dynamic forces depending on the surface wettability. Thus, the energy factor, which is defined as the ratio of the energy needed to form a bubble with a contact angle  $\theta$  on the surface to that needed to form a homogenous bubble with the same diameter, is believed to be the key parameter of the effects of the wetting on the bubble growth. Its expression is given by [30]:

$$f(\theta) = \frac{2 + 3 \cos \theta - \cos^3 \theta}{4} \quad (14)$$

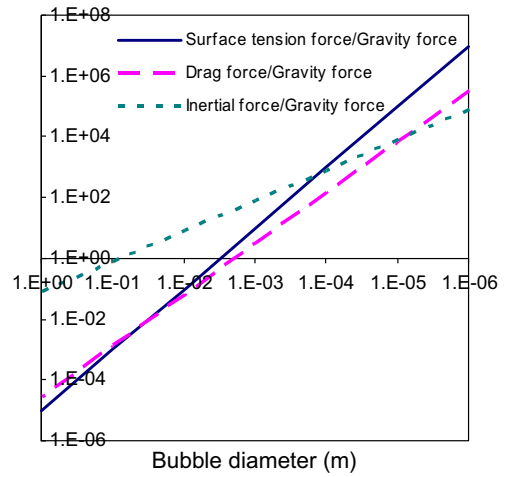


Fig. 18. Force balance for a bubble growth on the surface which has 30° static contact angle.

And the bubble formation energy is proportional to the energy factor as:

$$\Delta E_f(R^*, \theta) = \frac{4\pi R^{*2}}{3} \sigma \times f(\theta) \quad (15)$$

The energy factor can be easily understood as a volume ratio of the sphere which has a contact angle  $\theta$  on the surface and the full sphere which has the same diameter. Fig. 19 shows that this factor has the maximum value at 0° contact angle then decreases with the increase of the contact angle to reach the minimum value at 180°. Thus, the energy required to form initial vapour shape at a cavity is higher for a lower contact angle. This is the reason why the bubble is formed at very low heat flux for hydrophobic surfaces and why the waiting time increases with the enhancement of the surface wettability. Therefore, we established a new correlation of the bubble departure diameter which incorporates the influence of the fluid properties and the gravity as Fritz [20] did, but that also takes into account the energy factor as the contribution of the wetting effects:

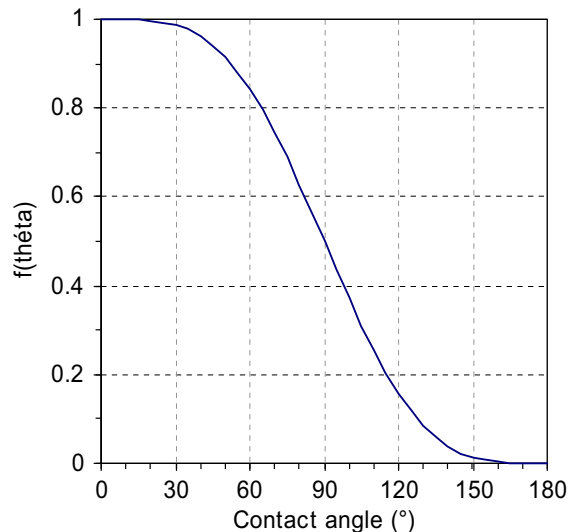


Fig. 19. Energy factor as a function of static contact angle.

$$D_b = 0.626977 \times \frac{(2 + 3 \cos \theta - \cos^3 \theta)}{4} \left( \frac{\sigma}{g(\rho_l - \rho_g)} \right)^{1/2}, \text{ for } \theta \leq 90^\circ \quad (16)$$

Fig. 20 shows that this new correlation fits the experimental results of this study relatively well with only 7% difference. Comparison with the data of studies [31–34] is presented in Fig. 21. As shown in Fig. 21a, most of the experimental data (90% of 28 data points) can be estimated by Eq. (16) with a maximum error of 25%. The correlation of Fritz [20] shows a bad agreement (cf. Fig. 21b). However, it should be mentioned that the correlation developed in this paper does not take into account the effects of superheat. Thus, further investigations are expected to optimise this correlation (with a physical model) and to validate it at a larger data set.

#### 4.4. Influence of the surface wettability on the HTC

Heat transfer from the wall to liquid through a bubble behaves differently depending whether the surface is wetted or not.

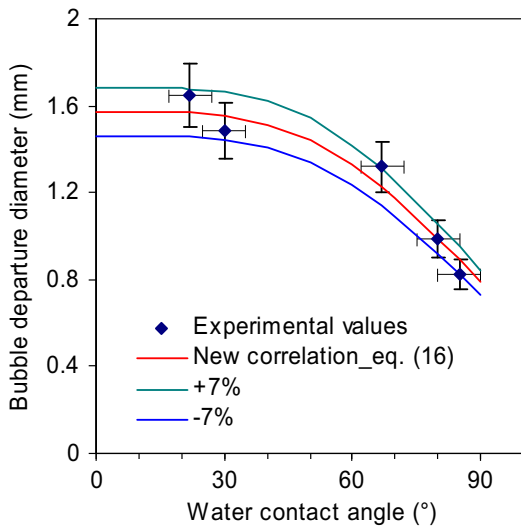
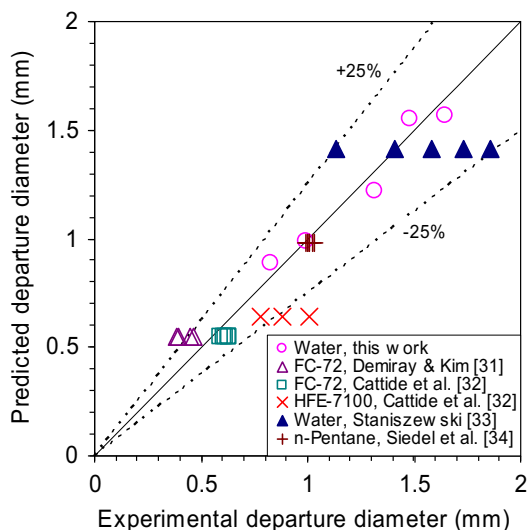
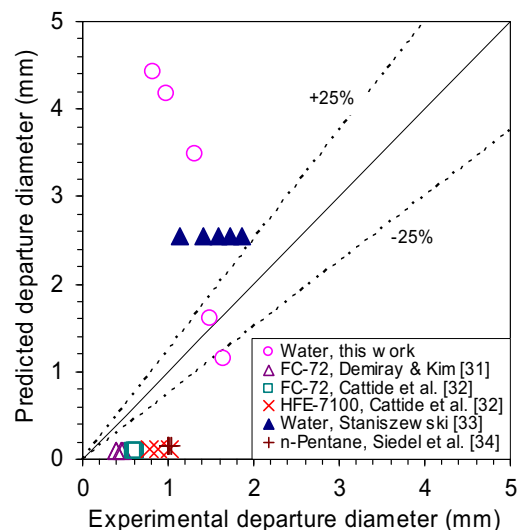


Fig. 20. New correlation to estimate the bubble departure diameter.



(a) Bubble departure correlation of this work



(b) Bubble departure correlation of Fritz [20]

Fig. 21. Comparison of predicted and measured vapour bubble departure diameter.

According to the three-zone model [35], hydrophilic surface has three different modes of heat transfer in zone I, II and III (cf. Fig. 22a). Zone I is the dry patch regime where no evaporation occurs. The heat transfer in this zone is relatively poor because of the poor conductivity of the vapour. Zone II is the conventional microlayer regime where very thin liquid layer evaporates to evacuate most of the heat coming from the wall. Zone III is an extended microlayer to bulk regime where the heat transfer is similar to that of single phase flow. For a hydrophobic surface, there is no liquid microlayer underneath the bubbles. The heat transfer occurs from superheat liquid layer [31] and through the dry patch zone (cf. Fig. 22b). The heat transfer in the dry patch zone is poor, causing local deterioration of the hydrophobic samples since bubbles are formed but do not detach from the wall.

Moreover, a classical way to enhance the HTC is to increase the bubble emission frequency. As the bubble emission frequency was observed to decrease with the wetting enhancement, the HTC should deteriorate when the contact angle reduces. Yet experimental results showed an excellent HTC with the surface that has a static contact angle close to either  $0^\circ$  or  $90^\circ$ . Indeed, for  $90^\circ$  contact angle surface, high HTC is obtained as a result of high bubble emission frequency. But for superhydrophilic surface, HTC enhances significantly by a larger and thinner liquid microlayer underneath the bubble where most of the heat pass through, even though the bubble emission frequency is lower compared to low wetted surfaces.

## 5. Conclusions

Subcooled pool boiling experiments were performed to study the effects of the surface wettability on nucleation mechanism and boiling heat transfer. Nano-surface coating that modifies the topography of the surface slightly has been used with the purpose of varying the static contact angle from  $22^\circ$  to  $112^\circ$ . The main results of this study are summarised as follows:

#### (a) Hydrophobic surfaces

- Bubble appears at the surface for a lower heat flux compared to the standard surfaces which are usually wetted.
- Bubbles cannot detach from the surface and coalesce with bubbles formed at neighbouring sites.

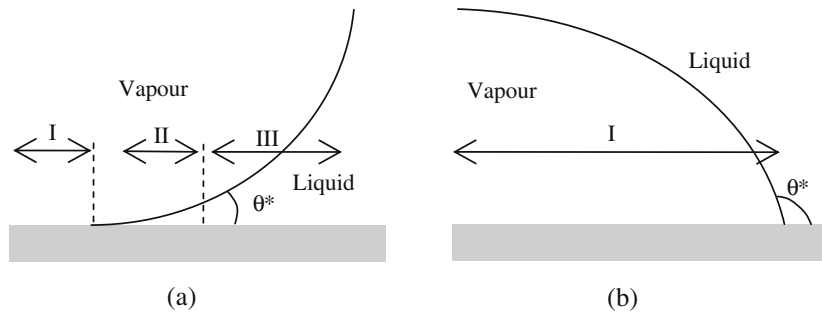


Fig. 22. Heat transfer zones on: (a) hydrophilic and (b) hydrophobic surfaces.

- The wall is locally deteriorated during the experiments by the presence of bubbles on its surface even at low heat flux (100–200 kW/m<sup>2</sup>).
- (b) Hydrophilic surfaces
- With the enhancement of the surface wettability, the bubble departure diameter increases whereas the bubble emission frequency decreases.
  - For weakly wetted surfaces ( $45^\circ < \theta < 90^\circ$ ), HTC deteriorates when the contact angle reduces. However, for very wetted surfaces ( $\theta \leq 45^\circ$ ), the inverse effect was observed: HTC improves with the increase of the wettability. Thus, we believe that the best HTC can be obtained not only at a contact angle close to  $90^\circ$  but also at a very low contact angle close to  $0^\circ$ .
- (c) Dynamic contact angle approach of the nucleation mechanism has been developed to better understand the observed phenomenon. The contact angle hysteresis was shown to play a very important role in the bubble growth.

### Acknowledgements

Special thanks to Stéphanie THOLLON and Thierry KREBS from the CEA LITEN/LTS laboratory for their technical support on the surface coating.

### References

- [1] V.P. Carey, *Liquid–Vapor Phase-Change Phenomena*, Taylor and Francis, 1992.
- [2] D.S. Wen, B.X. Wang, Effects of surface wettability on nucleate pool boiling heat transfer for surfactant solutions, *Int. J. Heat Mass Transfer* 45 (2002) 1739–1747.
- [3] S.P. Liaw, V.P. Dhir, Void fraction measurements during saturated pool boiling of water on partially wetted vertical surfaces, *J. Heat Transfer* 29 (2008) 731–738.
- [4] Y. Takata, S. Hidaka, J.M. Cao, T. Nakamura, H. Yamamoto, M. Masuda, T. Ito, Effect of surface wettability on boiling and evaporation, *Energy* 30 (2005) 209–220.
- [5] R.L. Webb, N.H. Kim, *Principles of Enhanced Heat Transfer*, Taylor and Francis, 2005.
- [6] P. Griffith, J.D. Wallis, The role of surface conditions in nucleate boiling, *Chem. Eng. Prog. Symp. Ser.* 56 (1960) 49–63.
- [7] R.F. Gaertner, Methods and means for increasing the heat transfer coefficient between a wall and boiling liquid, U.S. Patent 3301,314, 1967.
- [8] R.L. Hummel, Means for increasing the heat transfer coefficient between a wall and boiling liquid, U.S. Patent 3207,209, 1965.
- [9] R.L. Vachon, G.H. Nix, G.E. Tanger, Evaluation of constants for the Rohsenow pool-boiling correlation, *J. Heat Transfer* 90 (1968) 239–247.
- [10] J.S. Coursey, J. Kim, Nanofluid boiling: the effect of surface wettability, *Int. J. Heat Mass Transfer* 29 (2008) 1577–1585.
- [11] Z.H. Liu, L. Liao, Sorption and agglutination phenomenon of nanofluids on a plain heated surface during pool boiling, *Int. J. Heat Mass Transfer* 51 (2008) 2593–2602.
- [12] S.J. Kim, I.C. Bang, J. Buongiorno, L.W. Hu, Surface wettability change during pool boiling of nanofluids and its effect on critical heat flux, *Int. J. Heat Mass Transfer* 50 (2007) 4105–4116.
- [13] S. Khandekar, Y.M. Joshi, B. Metha, Thermal performance of closed two-phase thermosyphon using nanofluids, *Int. J. Therm. Sci.* 48 (2007) 815–824.
- [14] H.D. Kim, J. Kim, M.H. Kim, Experimental studies on CHF characteristics of nano-fluids at pool boiling, *Int. J. Multiphase Flow* 33 (2007) 691–706.
- [15] I.C. Bang, S.H. Chang, Boiling heat transfer performance and phenomena of Al<sub>2</sub>O<sub>3</sub>–water nano-fluids from a plain surface in a pool, *Int. J. Heat Mass Transfer* 48 (2005) 2407–2419.
- [16] S.K. Das, N. Putra, W. Roetzel, Pool boiling characteristics of nano-fluids, *Int. J. Heat Mass Transfer* 46 (2003) 851–862.
- [17] S. Thollon, F. Luc, M. Daturi, S. Valange, J. Barrault, Deposition of silver or silver alloy nanoparticles on substrate comprises use of organometallic precursors and deposition carried out in presence of reactive oxidant gas, Patent WO 2006070130.
- [18] M. Manin, S. Thollon, F. Emieux, G. Berthome, M. Pons, H. Guillon, Deposition of MgO thin film by liquid pulsed injection MOCVD, *Surf. Coat. Technol.* 200 (5–6) (2005) 1424.
- [19] N. Kolev, How accurately can we predict nucleate boiling, *Multiphase Flow Dynamics 2*, Springer, 2002.
- [20] W. Fritz, Maximum volume of vapour bubbles, *Phys. Z.* 36 (1935) 379–384.
- [21] L.Z. Zeng, J.F. Klausner, R. Mei, A unified model for the prediction of bubble detachment diameters in boiling systems – I. Pool boiling, *Int. J. Heat Mass Transfer* 36 (1993) 2261–2270.
- [22] R. Situ, M. Ishii, T. Hibiki, J.Y. Tu, G.H. Yeoh, M. Mori, Bubble departure frequency in forced convective subcooled boiling flow, *Int. J. Heat Mass Transfer* 51 (2008) 6268–6282.
- [23] R. Cole, A photographic study of pool boiling in the region of the critical heat flux, *AIChE J.* 6 (1960) 533–542.
- [24] N. Zuber, Nucleate boiling: the region of isolated bubbles and the similarity with natural convection, *Int. J. Heat Mass Transfer* 6 (1963) 53–78.
- [25] A.P. Hatton, I.S. Hall, Photographic study of boiling on prepared surfaces, in: *Third International Heat Transfer Conference*, vol. 4, Chicago, USA, pp. 24–37, 1966.
- [26] H.J. Ivey, Relationships between bubble frequency, departure diameter and rise velocity in nucleate boiling, *Int. J. Heat Mass Transfer* 10 (1967) 1023–1040.
- [27] M.G. Cooper, Heat flows rates in saturated pool boiling – a wide ranging examination using reduced properties, *Advanced in Heat Transfer*, Academic Press, Orlando, Florida, 1984.
- [28] R.N. Wenzel, Surface roughness and contact angle (letter), *J. Phys. Colloid Chem.* 53 (9) (1949) 1466.
- [29] F.N. Peebles, H.J. Garber, Study on the motion of gas bubbles in liquids, *Chem. Eng. Prog.* 49 (1953) 88–97.
- [30] S.G. Bankoff, Ebullition from solid surfaces in the absence of a pre-existing gaseous phase, *Trans. Am. Mech. Eng.* 79 (1957) 735–740.
- [31] F. Demiray, J. Kim, Microscale heat transfer measurements during pool boiling of FC-72: effect of subcooling, *Int. J. Heat Mass Transfer* 47 (2004) 3257–3268.
- [32] A. Cattide, G.P. Celata, P. Di Marco, W. Grassi, Experimental study on bubble detachment under variable heat load and the action of electric field, *Fluid Dyn. Res.* 40 (2008) 485–496.
- [33] B.E. Staniszwski, Bubble growth and departure in nucleate boiling, *Tech. Rept. No. 16*, MIT, Cambridge, Mass, 1959.
- [34] S. Siedel, S. Cioulachtjian, J. Bonjour, Experimental analysis of bubble growth, departure and interactions during pool boiling on artificial nucleation sites, *Exp. Therm. Fluid Sci.* 32 (2008) 1504–1511.
- [35] P.C. Wayner, Intermolecular forces in change of phase heat transfer: 1998 Donald Q. Kern award review, *AIChE J.* 45 (1999) 2055–2068.